

# Combination anti-PD-1 and electroacupuncture induces a potent anti-tumor immune response in microsatellite-stable colorectal cancer

**Running title:** EA enhances the efficacy of anti-PD-1 in MSS CRC

Yuan Wang<sup>1,2,3,#</sup>, Fengyi Liu<sup>4,5,#</sup>, Xiaoxue Du<sup>1,2,3,#</sup>, Jiaqi Shi<sup>2,3,#</sup>, Rui Yu<sup>6</sup>, Shuang Li<sup>1,3</sup>, Ruisi Na<sup>1,2,3</sup>, Ying Zhao<sup>1,2,3</sup>, Meng Zhou<sup>1,2,3</sup>, Ying Guo<sup>3</sup>, Liang Cheng<sup>7</sup>, Guangyu Wang<sup>1,2</sup>, Tongsen Zheng<sup>1,2,3,8,\*</sup>

## Affiliations

<sup>1</sup> Department of Gastrointestinal Medical Oncology, Harbin Medical University Cancer Hospital, No. 150 Haping Road, Nangang District, Harbin 150081, P. R. China.

<sup>2</sup> Department of Phase 1 Trials Center, Harbin Medical University Cancer Hospital, No. 150 Haping Road, Nangang District, Harbin 150081, P. R. China.

<sup>3</sup> Heilongjiang Province Key Laboratory of Molecular Oncology, No. 150 Haping Road, Nangang District, Harbin, Heilongjiang Province 150081, P. R. China.

<sup>4</sup> Department of Integrated Traditional Chinese and Western Medicine, First Affiliated Hospital of Harbin Medical University, Harbin 150001, P. R. China.

<sup>5</sup> Heilongjiang University of Chinese Medicine, No.24, Heping Road, Xiangfang District, Harbin, 150040, P. R. China.

<sup>6</sup> College of Bioinformatics Science and Technology, Harbin Medical University, Harbin, Heilongjiang, 150081, P. R. China.

<sup>7</sup> College of Bioinformatics Science and Technology, NHC Key Laboratory of Molecular Probe and Targeted Diagnosis and Therapy, Harbin Medical University,

Harbin, Heilongjiang, 150081, P. R. China.

<sup>8</sup> Heilongjiang Cancer Institute, No. 150 Haping Road, Nangang District, Harbin  
150081, P. R. China.

# **The authors shared the first authorship.**

\* **Corresponding author**

**Keywords:** Colorectal cancer, Immunotherapy, Electroacupuncture, Anti-tumor  
immune response

**Funding:** This work was supported by the National Natural Science Foundation of  
China (U20A20377 and 81872435); “Tou Yan” Action of Heilongjiang province; and  
the HMU Marshal Initiative Funding (HMUMIF-21004)

**Corresponding author information:**

Name: Tongsen, Zheng

Address: Department of Gastrointestinal Medical Oncology, Harbin Medical  
University Cancer Hospital, No. 150 Haping Road, Nangang District, Harbin 150081,  
P. R. China

Phone number: +86-451-86298203

Fax: +86-451-86298278

E-mail address: [zhengtongsen@hrbmu.edu.cn](mailto:zhengtongsen@hrbmu.edu.cn)

**Conflicts of Interest:** The authors declare no potential conflicts of interest.

**Synopsis:** Electroacupuncture (EA) is demonstrated to inhibit microsatellite-stable  
colorectal cancer (MSS CRC) progression and enhance efficacy of anti-PD-1 by  
boosting antitumor responses. Combination EA and anti-PD-1 is highlighted as a

feasible and safe treatment option for MSS CRC.

## Abstract

Programmed death receptor-1 (PD-1) inhibitors are ineffective against microsatellite-stable (MSS) colorectal cancer (CRC). Electroacupuncture (EA) has onco-suppressive and immunomodulatory properties. Here, we investigated the anti-tumor effects of EA and explored the feasibility of EA combined with anti-PD-1 in MSS CRC. Results showed that EA exerted its anti-tumor effect in an intensity-specific manner, and moderate-intensity EA (1.0 mA) induced maximal tumor inhibition. EA enhanced anti-tumor immune responses by increasing lymphocytes and granzyme B (GzmB) levels, as well as activating the stimulator of interferon genes (STING) pathway. EA combined with anti-PD-1 showed superior efficacy compared with either monotherapy in multiple MSS CRC mouse models. Single-cell RNA sequencing revealed that cotreatment reprogrammed the tumor immune microenvironment (TIME), as characterized by enhancement of cytotoxic functions. Mechanically, we found the potentiated effect of EA was dependent upon the STING pathway. Collectively, EA reshapes the TIME of MSS CRC and sensitizes tumors to anti-PD-1 in a STING pathway-dependent manner. These results provide a mechanistic rationale for using EA as an immunomodulatory strategy to improve the clinical efficacy of anti-PD-1 in MSS CRC. EA is safe, well-tolerated, and feasible for clinical translation as a promising strategy for treating MSS CRC.

## Introduction

Colorectal cancer (CRC) is the third most commonly diagnosed cancer and the second leading cause of cancer-related mortality worldwide (1). Immune checkpoint inhibitors (ICIs) targeting PD-1/PD-L1 have revolutionized microsatellite-instable CRC treatment (2, 3). However, single-agent ICIs are ineffective for patients with microsatellite stable (MSS) molecular phenotype, comprising about 80-85% of cases (4). MSS CRC, classified as an immune-desert tumor, lacks tumor-infiltrating lymphocytes, which hampers anti-tumor immune responses. Recent research attributes primary immunotherapy resistance in MSS CRC to its immunosuppressive tumor microenvironment (TME) armed with various immune escape mechanisms (5). Efforts to overcome this resistance through combination therapies involving chemo/radiotherapy, MEK inhibitors, VEGF/R inhibitors, WNT/ $\beta$ -catenin inhibitors, and oncolytic viruses have not yielded significant benefits (5, 6). Therefore, research on immunomodulatory strategies that could surmount the inherent resistance to ICIs observed in MSS CRC is urgently required.

Electroacupuncture (EA) is a valuable complementary and alternative medicine with attributes of safety, affordability, and minimal adverse effects (7, 8). Its effect is based on factors like acupoint selection, frequency, and current intensity (9). Regarding cancer treatment, EA is extensively employed to alleviate cancer-related symptoms and side-effects of treatment in clinical practice (10-12). Recent findings using various EA intensities indicate that EA exerts direct anti-tumor and potent immunomodulatory effects via the neural-endocrine-immune network (11, 13).

Emerging evidence suggests that EA reduces tumor burden in preclinical studies (10, 13, 14). Moreover, EA restores immune function of patients with malignant tumors by increasing lymphocytes and regulating inflammatory cytokines (11, 15). In this context, EA appears to be a suitable strategy for enhancing immunotherapy response in MSS CRC. Here, we tested the hypothesis that EA can remodel the TME and has the potential to synergize with anti-PD-1 therapy in MSS CRC.

In this study, we first found that EA reduced MSS tumor growth in an intensity-specific manner and improved the efficacy of anti-PD-1 in multiple syngeneic mouse models of MSS CRC. Mechanically, EA combined with anti-PD-1 reshaped TME and substantially enhanced anti-tumor immune responses. In addition, the synergism between EA and anti-PD-1 was dependent on the activation of the STING signaling pathway. This study highlights combination EA and anti-PD-1 as a promising approach to treating MSS CRC.

## **Methods and Materials**

Details for reagents are in the supplement.

### **Cell lines**

The murine colon cancer cell line CT26 was purchased from Wuhan Pu-nuo-sai Life Technology Co. Ltd. (Wuhan, China) in 2022. CMT93 was obtained from ATCC in 2022. CT26-luc cells were generated by retroviral transduction in CT26 cells. **The**

pLent-Puro-CMV-luciferase lentiviral vectors (Vigene Biosciences) were used to package the viral particles. Next, the CT26 cell line was infected with this virus. Both stably transformed, overexpressing luciferase gene- and mock-infected cells were selected with puromycin (1 µg/mL, Sigma-Aldrich).

Both CT26 and CT26-luc cell lines were cultured at 37°C in RPMI-1640 medium (Gibco, California, USA) supplemented with 10% fetal bovine serum (Gibco) and 1% penicillin/streptomycin antibiotics (Biyuntian Biotechnology) under 5% CO<sub>2</sub>. CMT93 was cultured at 37°C in DMEM (Gibco) with 10% fetal bovine serum (Gibco) and 1% penicillin/streptomycin (Biyuntian Biotechnology) under 5% CO<sub>2</sub>. Cells were digested with pancreatin (Biyuntian Biotechnology) and stored in a serum-free cell cryopreservation medium (NCM Biotech). CT26 and CT26-luc were subcultured every two days and CMT93 was subcultured every three days. Experiments were carried out within 6 months after the acquisition of the cell lines. Cells were passaged three to four times post-thaw before implanting into mice. All cell lines were validated by STR DNA fingerprinting every 6 months. DNA was isolated using the Axygen Axy Prep DNA Gel Extraction kit (Axygen, Shanghai, China). Mycoplasma contamination was ruled out using a PCR-based detection kit (PromKine, PK-CA91-1048) every 3 months.

## Mice

BALB/c mice (female, 5 weeks old), C57BL/6 (female, 5 weeks old) mice, and NYG mice (female, 5 weeks old) were purchased from Changsheng Biotechnology.

STING-deficient (*Tmem173<sup>8t</sup>*) mice, generated by a forward genetic mutagenesis screen in C57BL/6J mice using the mutagen N-ethyl-N-nitrosourea, were purchased from the Jackson Laboratory. All animal studies were conducted with the approval of Harbin Medical University's Institutional Animal Care and Use Committee (HMUIRB2023019), in compliance with the ARRIVE guidelines for the care and use of laboratory animals. All mice were bred and maintained in-house on a regulated 12 hours a day/night cycle.

### **Colorectal cancer subcutaneous models**

For subcutaneous tumor models,  $2 \times 10^5$  CT26 cells were injected subcutaneously in the flank of BALB/c and NYG mice.  $1 \times 10^6$  CMT93 cells were injected subcutaneously in the flank of C57BL/6 and STING-deficient (*Tmem173<sup>8t</sup>*) mice. When tumor volume reached around 100-200 mm<sup>3</sup>, we started 2 weeks of treatment in all colorectal cancer subcutaneous models. EA stimulation was applied at bilateral ST36, located 5 mm below the fibular head and posterolateral to the knee. EA was performed 30 minutes daily, once a day. Mice in the sham-operated group were treated with the same acupoints, but no current was applied. Mice in the control groups were fixed similarly without EA intervention. EA stimulation was applied with intensities of 0.5, 1.0, or 1.5 mA and a frequency of 10 Hz, as the previous study described (9, 11). The anti-PD-1 and combination groups of mice were intraperitoneally injected with 100µg anti-PD-1 (Bioxell, Clone: RMP1-14, BE0146) every two days. Sterilized acupuncture needles were purchased from Zhongyan Taihe



Co. (Beijing, China). EA intervention was performed using Han's Point-Nerve Stimulator Instrument (Hans, LH202H).

Tumor growth and survival were assessed. Tumor size was determined using electronic calipers to measure the length and width and calculated by  $L \times W^2/2$ . The tumor size and body weight were recorded on alternate days. Mice were followed for 2 weeks, and then blood (via retro-orbital plexus) and tumors were collected for analysis. For survival analysis, the survival period was calculated from the day of inoculation of cancer cells to the day of death of the mouse. All mice were monitored every two days for death. When mice were observed with a tumor volume reaching  $\sim 2000 \text{ mm}^3$ , signs of tumor necrosis, or greater than 20% weight loss, the mice were euthanized. The survival protocol lasted nearly two months after inoculation.

### **Colorectal cancer orthotopic model**

The orthotopic colon cancer model was performed as previously described in wild-type BALB/c (16). Briefly, all mice were injected with  $2 \times 10^5$  CT26-luc cells. A total volume of 50  $\mu\text{L}$  of a cell suspension was injected into the cecal wall using an insulin-gauge syringe. The abdominal access in mice was made through a 1 cm hypogastric midline skin and peritoneal wall incision. The caecum was gently exteriorized, and tumor cells were injected as described. The caecum was returned to the peritoneal cavity, and the peritoneum and skin were closed by running sutures and wound clips. D-luciferin potassium salt (Gold biotechnology, LUCK-1G) was used for visualizing the cells by fluorescence. D-Luciferin potassium salt (5 mg/mouse in

100  $\mu$ L PBS) was intraperitoneally injected within 15 min post injection to guarantee a steady light emission, and luminescence was detected using the IVIS Lumina LT Series III *in vivo* imaging system (CLS136334, PerkinElmer) under isoflurane anesthesia (RWD Life Science, R510-22). Anesthesia was maintained with 1.5% isoflurane in oxygen delivered at 1 L per min. Mice were imaged twice a week and randomly divided into four groups for treatments when tumors fluorescence value reached  $\sim 1 \times 10^4$  (p/s). The treatment regimen was consistent with colorectal cancer subcutaneous models. All of the mice were maintained until death caused by the neoplastic process or until two weeks of treatment end.

### **Tumor dissociation**

Tumor tissues were isolated from CT26 subcutaneous tumor model and cut into small sections ( $\sim 2$ mm pieces). A digestion enzyme solution was prepared as follows: collagenase IV (1 mg/mL; Solarbio, C8160), hyaluronidase (0.1 mg/mL; Solarbio, H8030), DNase I (0.1 mg/mL; Solarbio, D8071). Approximately 5 mL of digestion enzyme solution was prepared per tissue sample. The tissue samples were incubated in the digestion enzyme solution at 37°C with 160r/min continuous agitation for 60 min. Cells were passed then through a 70  $\mu$ m filter (Biosharp, BS-70-CS), then digestion was stopped with PBS. Red blood cells were lysed with a five-fold volume of red blood cell lysis buffer (TBD, NH4CL2009). For RNA sequencing, tumor tissues from CT26 subcutaneous tumor model were digested with 2 mL sCellLive<sup>TM</sup> Tissue Dissociation Mix (Singleron Biotechnologies) solution using the Singleron

PythoN™ Automated Tissue Dissociator (Singleron Biotechnologies) at 37°C for 15min. The tissue lysate was centrifuged at 500×g for 5 min, and the pellet was suspended with PBS.

### **Flow cytometry (FCM)**

Tumor tissues were isolated from CT26 subcutaneous tumor model and processed into a single-cell suspensions as described above. Red blood cells were lysed with a five-fold volume of red blood cell lysis buffer (TBD, NH<sub>4</sub>CL2009). Dead cells were excluded using the Zombie NIR Fixable Viability kit (Biolegend, 423106). After washing with PBS, cells were stained with surface antibodies specific to anti-CD45 (Biolegend, 103108), anti-CD3 (Biolegend, 100328), anti-CD11b (Biolegend, 101228), anti-CD8a (Biolegend, 100708), anti-CD49b (Biolegend, 108907), anti-Gr-1 (Biolegend, 108412) at 4 °C for 30 min. CD8<sup>+</sup> T cells were defined as CD45<sup>+</sup>CD3<sup>+</sup>CD8a<sup>+</sup> cells. NK cells were defined as CD45<sup>+</sup>CD3<sup>-</sup>CD49b<sup>+</sup> cells. NKT cells were defined as CD45<sup>+</sup>CD3<sup>+</sup>CD49b<sup>+</sup> cells. MDSCs were defined as CD45<sup>+</sup>CD11b<sup>+</sup>GR-1<sup>+</sup> cells. For intracellular GzmB stimulation and block, rapidly thawed BD GolgiPlug™ Leukocyte Activation Cocktail (Fisherscientific, BD 550029) in a 37°C water bath was used. 0.2 µL of the cocktail was added to every 100 µL of cell culture (10<sup>6</sup> cells/mL) and mixed thoroughly. The cells were incubated at 37°C in a humidified CO<sub>2</sub> incubator at 37 °C for 6 hours. Subsequently, intracellular staining was performed using anti-GzmB (Biolegend, 372214) after fixation using the Fixation/Permeabilization Solution kit (Absin, abs9110), and anti-GzmB was

incubated in the dark at 4 °C for 30 min. Mouse IgG1,  $\kappa$  isotype ctrl antibody (Biolegend, 400126) was additionally used. Single-cell suspensions were analyzed with a BD FACS Aria flow cytometer (BD, FACSMelody™). Data was analyzed offline using FlowJo analysis software (FlowJo, LLC).

### **Immunohistochemistry (IHC)**

The CT26 tumors were cut into 4.0  $\mu\text{m}$  sections and then dried. The slices were incubated at 4°C overnight with different antibodies, including PD-L1 (1:500, Cell Signaling Technology, 64988), GzmB (1:10000, Abcam, Ab140211), and IFN- $\beta$  (1:400, Abcam, Ab255598). Slices were incubated with corresponding secondary antibodies for 30 minutes. The secondary antibodies used were goat anti-rabbit (ZSGB-BIO, PV-6001) for PD-L1 and IFN $\beta$ , and goat anti-mouse (ZSGB-BIO, PV-6002) for GzmB. Images of stained slices were collected by a Digital Slide Scanner (Motic, Canada). Two pathologists evaluated all cases independently without prior knowledge of the experimental data or the grouping. After staining, five images of each section were randomly selected for evaluation of staining scores. Two independent observers performed immunostaining scores on 100 epithelial cells in each image, ranging from 0 (unstained) to 3 (strongly stained). The intensity score was as follows: 0, negative; 1, Weak; 2, Mild; 3, strong. The frequency of positive cells was defined as follows: 0, less than 5%; 1, 5% - 25%; 2, 26% -50%; 3, 51% -75%; 4, greater than 75%. A positive reaction was defined as a brown signal displayed in the cytoplasm. The staining index was determined by multiplying the

staining intensity score by the positive area score.

### **Enzyme-linked immunosorbent assay (ELISA)**

Blood was extracted from CT26 subcutaneous tumor model at the experimental endpoint by retro-orbital bleeding, left to stand at room temperature for 60 min, and serum was then collected following centrifugation at 5,000xg for 30 min at 4 °C. Subsequently, serum was analyzed using ELISA kits for IFN- $\beta$  (PBL Assay Science, 42400-1), adrenaline (Elabscience Biotechnology, E-EL-0045c), noradrenaline (NA) (Elabscience Biotechnology, E-EL-0047c), and dopamine (Elabscience Biotechnology, E-EL-0046c) according to the manufacturer's instructions. 50-100  $\mu$ L serum was added into each well following the manufacturer's instructions. Standard curve was defined according to the kit's instructions and standard dilutions. Absorbance was measured at 450 nm on the Tecan microplate reader (Tecan) and calculated using ELISAcac. A standard curve with NA, adrenaline, dopamine, or IFN $\beta$  was performed with each assay, respectively. All samples were assayed in duplicate.

### **Quantitative real-time PCR (qRT-PCR)**

Total RNA of CT26 tumors from subcutaneous tumor model was extracted by Trizol. Reverse transcription was performed using PrimeScript™ RT reagent Kit. Quantitative real-time PCR was carried out with a 7500 Real-time PCR system (Applied Biosystems, USA) using a FastStart Universal SYBR Green Master kit. 20ng cDNA template sample were used for reaction and each sample contained three

replicates. PCR primers are detailed in Supplementary Table S1. The expression of different genes was detected using the gene for  $\beta$ -actin as the control. Expression was calculated by the  $\Delta\Delta C_t$  method.

### **Western blotting (WB)**

Tumor tissues were isolated from CT26 subcutaneous tumor model and lysed in a RIPA buffer (Biyuntian Biotechnology, P0013B) for 20 minutes on ice. Lysis was followed by a 15min centrifugation to pellet the nuclei and insoluble materials. The supernatants were subsequently used as indicated. The protein concentration was assessed using a BCA assay (Biyuntian Biotechnology, P0012). In each lane, 120  $\mu$ g of protein was loaded onto a 10% gel. GAPDH (1:500, Absin, abs830030) was used as a loading control. The tumor extracts were separated by 10% SDS polyacrylamide gel electrophoresis (EpiZyme Biotechnology, PG112) and transferred to a nitrocellulose membrane (BioTrace NT, PALL Corp, 66485). The following primary antibodies were used: TBK1/NAK (1:1000, Cell Signaling Technology, 3504), phospho-TBK1/NAK (1:1000, Abcam, Ab109272), IRF3 (1:1000, Abcam, Ab68481), and phospho-IRF3 (1:1000, Cell Signaling Technology, 29047). Secondary antibodies used included goat anti-Mouse IgG DyLight 680 (1:800, Abbkine Scientific, A23710) and goat anti-rabbit IRDye 800CW (1:8000, Licor, 925–32211). The fluorescent gel was imaged on a BioRad ChemiDoc MP Imaging System.

### **Bulk RNA-sequencing (RNA-seq)**

Tumor tissues in the control and EA group (1.0 mA) were isolated from CT26 subcutaneous tumor model. Each group included three mice. CT26 tumor tissues were dissociated into single-cell suspensions as indicated above. Total RNA was isolated using RNeasy mini kit (Qiagen, Germany). Total RNA was quantified using a NanoDrop ND-2000 (Thermo Fisher Scientific). Integrity of total RNA was assessed using the Agilent 2100 Bioanalyzer (Agilent Technologies Inc., USA), and samples with RNA integrity number (RIN) values above 7.0 were used for sequencing. 1 µg of RNA were used as input material for the RNA sample preparations.

Paired-end libraries were synthesized by using the mRNA-seq Lib Prep Kit for Illumina (ABclonal, China) following Sample Preparation Guide. Briefly, the poly-A containing mRNA molecules were purified using poly-T oligo-attached magnetic beads. Following purification, the mRNA was fragmented into small pieces using divalent cations under 94°C for 8 min. The cleaved RNA fragments were copied into first-strand cDNA using reverse transcriptase and random primers. This was followed by second-strand cDNA synthesis using DNA Polymerase I and RNase H. We then performed end repair processing on the cDNA fragments, a single 'A' base was added, and then ligation of the adapters was performed. The products were then purified and enriched with PCR to create the final cDNA library. Purified libraries were quantified by Qubit® 2.0 Fluorometer (Life Technologies, USA) and validated by Agilent 2100 bioanalyzer (Agilent Technologies, USA) to confirm the insert size and calculate the mole concentration. Cluster was generated by cBot with the library diluted to 10 pM and then samples were sequenced on the Illumina NovaSeq 6000 (Illumina, USA).

Paired-end sequence files (fastq) were mapped to the reference genome (GRCm38.102) using Hisat2 (Hierarchical Indexing for Spliced Alignment of Transcripts, version 2.0.5). The output SAM (sequencing alignment/map) files were converted to BAM (binary alignment/map) files and sorted using SAMtools (version 1.3.1). Quality control criteria: data volume of approximately 15G per sample, with a proportion of bases having a quality score greater than 20 (Q20) not less than 90%. Gene abundance was expressed as fragments per kilobase of exon per million reads mapped (FPKM). Stringtie software was used to count the fragment within each gene, and TMM algorithm was used for normalization. Differential expression analysis for mRNA was performed using R package (version 3.4.3) edgeR. Differentially expressed RNAs with  $|\log_2(\text{FC})|$  value  $>1.5$ , q value  $<0.05$  and one group's mean FPKM  $>1$ , considered as significantly modulated, were retained for further analysis. We performed a Gene Ontology (GO) analysis for biological processes, cellular components and molecular function and a KEGG pathway analysis (Kyoto Encyclopedia of Genes and Genomes <http://www.genome.ad.jp/kegg>) via enrich R package (version 3.4.3). Bulk RNA-sequencing was carried out by Sinotech Genomics Corporation.

### **Single-cell RNA sequencing (scRNA-seq)**

Tumor tissues in the control, EA (1.0 mA), anti-PD-1, and combination groups were isolated from the CT26 subcutaneous tumor model. CT26 tumor tissues were dissociated into single-cell suspensions as indicated above. The sample was stained



with trypan blue (Sigma, Shanghai, China) and microscopically evaluated for cell viability. Libraries were prepared using Chromium Single Cell 3' Reagent Kits v3.1 according to manufacturer's protocol (10X Genomics). The generated scRNA-seq libraries were sequenced on Illumina novaseq6000 with 150 bp paired-end reads. 10  $\mu$ L cDNA template was used for reaction. The Cell Ranger Single-Cell Software Suite (V.6.1.0) was used to perform sample demultiplexing, barcode processing, and single-cell gene counting. The number of cells in each group was 6303 in the control group, 8426 in the EA group, 14582 in the anti-PD-1 group, and 12506 in the combination group. A mean tumor sequencing depth of 38K was achieved. Reference genome (GRCm38.102) was used for alignment. Further analyses, including quality control, identification of highly variable genes, dimensionality reduction, standard unsupervised clustering algorithms, and the discovery of differentially expressed genes, were performed using the Seurat package in R (V.4.2.1). To remove dead cells, transcriptomes were filtered for cells with 500-10,000 genes detected, 1000-100,000 UMIs counted, fraction of mitochondrial reads <30%, and fraction of hemoglobin reads <5%. scRNA-seq was carried out by Singleron Biotechnologies Corporation.

### **Statistical analysis**

Data are presented as mean  $\pm$  SEM and were analyzed using GraphPad Prism Software version 8.0 (GraphPad, La Jolla, California, USA). To compare two groups, statistical significance was determined by a two-tailed unpaired Student's t-test; to compare multiple groups, one-way analysis of variance (ANOVA) followed by

Tukey's multiple comparisons test was performed. Treatment effects on tumor growth were evaluated by a two-way ANOVA with Dunnett's multiple comparisons test. Cumulative survival time was estimated by the Kaplan-Meier method, and the log-rank test was applied to compare the groups. A *P* value of < 0.05 was considered statistically significant (\**P* < 0.05; \*\**P* < 0.01; \*\*\**P* < 0.001).

### **Data Availability**

The data that support the findings of this study are available from the corresponding author upon reasonable request. All RNA-sequencing raw data generated in this study have been deposited in Sequence Read Archive (SRA) database and are accessible through accession number PRJNA1021342. For details regarding reagents, please see the Supplementary Table S2.

### **Results**

#### **Electroacupuncture inhibits MSS CRC tumor growth in an intensity-specific manner and improves anti-tumor immunity**

Previous studies demonstrate that low frequencies of EA improve immune functions in patients with malignancies (11). However, the intensity of EA employed varies across studies, ranging from 0.1 to 2.0 mA (11). Therefore, we first evaluated the anti-tumor effects of the frequently employed and safe intensities (0.5, 1.0, and 1.5 mA) in a subcutaneous CT26 mouse MSS CRC model. BALB/c mice were given

sham EA or varying intensities of EA once a day for 14 days (**Fig. 1A**). Results demonstrated that EA induced significant suppression of tumor growth at 1.0 mA and modest suppression at 0.5 mA and 1.5 mA (**Fig. 1B-C**; Supplementary Fig. S1A). In this context, a moderate current intensity induced the most significant tumor inhibition, indicating that efficacy does not always increase with intensity. The results revealed that EA exerts its anti-tumor effect in an intensity-specific manner.

To dissect the effect of EA on anti-tumor immunity, we first used FCM analyses to detect and quantify immune cell subsets. The 1.0 mA EA was selected for subsequent experiments due to its substantial tumor-suppressive effect. We found CD8<sup>+</sup> T cells and NK cells were significantly increased in the TME and blood, whereas myeloid-derived suppressor cells (MDSCs) were reduced (**Fig. 1D-E**; Supplementary Fig. S1B). To explore the mechanism, we performed RNA sequencing in CT26 tumors from control and EA groups. KEGG enrichment analysis showed that significantly changed genes were most often enriched in the immune and endocrine systems (Supplementary Fig. S1C). Previous studies have shown that EA modulates innate immune responses by releasing catecholamines (8). Here, we identified a notable decrease in serum NA after EA, whereas this effect was not observed for dopamine and noradrenaline (**Fig. 1F**).

GO analysis further revealed the activation of innate immune responses, such as granzyme-mediated programmed cell death signaling, granzyme-mediated apoptotic signaling, and response to interferon-beta (IFN- $\beta$ ) (**Fig. 1G**). We performed protein-protein interaction (PPI) analysis to identify key proteins in enriched immune

pathways, pinpointing PD-L1 as the hub gene (Supplementary Fig. S1D). Subsequently, protein levels of GzmB, PD-L1, and IFN $\beta$  in CT26 tumors were assessed via IHC and ELISA, and mRNA expression was measured through qRT-PCR. Results showed a significant upregulation of GzmB, PD-L1, and IFN $\beta$  expression in EA group (**Fig. 1H-J**). Given that the STING pathway plays a crucial role in producing IFN $\beta$ , we next examined whether the STING pathway was activated. We observed an increase in phosphorylated IRF3 (pIRF3) and TBK1 (pTBK1) (**Fig. 1K**).

To summarize, EA treatment significantly enhanced anti-tumor immunity by increasing the infiltration of lymphocytes, elevating GzmB expression, and activating the STING pathway. In addition, the expression of PD-L1 was upregulated due to immune activation in TME. These findings raised the possibility that the combination of EA and anti-PD-1 therapy could synergistically suppress MSS CRC growth.

### **Electroacupuncture enhances efficacy of anti-PD-1 in multiple MSS CRC models**

We first used CT26 and CMT93 subcutaneous tumor models to test the treatments. Tumor-bearing mice were treated with 1.0 mA EA, anti-PD-1, or EA combined with anti-PD-1 (EA+aPD1) for 14 days (**Fig. 2A**; Supplementary Fig. S2A). EA treatment at the indicated intensity led to tumor regression, whereas no significant suppression of tumor growth in mice treated with anti-PD-1 was observed (**Fig. 2B**; Supplementary Fig. S2B). The EA+aPD1 treatment showed a stronger anti-tumor efficiency than either monotherapy (**Fig. 2C**; Supplementary Fig. S2C). This result was confirmed by fold-change in tumor volume for each group (**Fig. 2D**;

Supplementary Fig. S2D). In addition, there was no significant difference in the weight of mice among groups, confirming an excellent safety profile (Supplementary Fig. S2E-F). Of note, the mice treated with EA+aPD1 also survived longer than other groups (**Fig. 2E**; Supplementary Fig. S2G), suggesting a better survival benefit in the EA+aPD1 group. Next, we evaluated the effect of EA+aPD1 on innate immune responses. As we expected, IHC of tumor tissues revealed the upregulated expression of GzmB in EA and combination groups (Supplementary Fig. S2H). Thus, EA not only exerted an anti-tumor effect but also significantly enhanced the efficacy of anti-PD-1 in syngeneic mouse models of MSS CRC. Next, we also used an orthotopic CRC model to confirm the potentiated effects of EA. Compared to the control group, both EA and combined treatment significantly decreased fluorescence intensity, with EA notably boosting the therapeutic effects of anti-PD-1 treatment (**Fig. 2F-G**). Taken together, these data support that EA robustly enhances anti-PD-1 therapy in MSS CRC.

### **Single-cell RNA sequencing validates the enhanced anti-tumor immunity in the combination group**

To further examine how EA+aPD1 affected the tumor immune microenvironment, scRNA-seq was conducted with the 10x chromium method. After quality control and filtering, single-cell transcriptomes from 32076 cells, with a median of 1514 genes, were obtained. Clustering analysis revealed 10 cell populations in the tumors of treated mice. Nine cell types with unique transcription features were identified

(Supplementary Fig. S3A), including fibroblasts (*Dcn*, *Igfbp7*, *Coll1a2*, and *Coll1a1*), mast cells (*Kit*, *Tpsab1*, and *Tpsb2*), granulocytes (*SI00a8* and *SI00a9*), macrophages (*Cl1qc*, *Cl1qa*, *Cl1qb*, and *Cd68*), B cells (*Cd79a* and *Ms4a1*), NK cells (*Nkg7*, *Klrk1*, *Klrk1*, and *Ncr1*), NKT cells (*Cd3*, *Nkg7*, and *Ncr1*), CD8<sup>+</sup> T cells (*Cd3* and *Cd8*), and regulatory T cells (Tregs; *Cd3*, *Cd4*, and *Foxp3*). We visualized these populations in two-dimensional spaces using t-SNE (**Fig. 3A**). The proportions of cell types differed significantly among the four groups. The combination group had the fewest tumor cells compared with other groups (Control: 93.04%, anti-PD-1: 91.07%, EA: 90.08%, EA+aPD1: 83.28%). Importantly, the proportions of T lymphocytes and NK cells were dramatically increased in the EA and combination groups (**Fig. 3B**; Supplementary, Fig. S3B-C). After that, we utilized FCM to confirm the increased infiltration of NK cells, NKT cells, and CD8<sup>+</sup> T cells that was observed in the single-cell analysis (**Fig. 3C**; Supplementary Fig. S4; Supplementary Fig. S5A).

Due to increased GzmB expression in the EA and combination groups, we next aimed to identify the sources of GzmB. Single-cell analysis revealed NKT cells and NK cells as primarily GzmB expressors (**Fig. 3D**). Notably, the adrenergic-like receptors *Adrb1* and *Adrb2* were predominantly present on the surface of NKT cells, followed by NK cells and CD8<sup>+</sup> T cells (**Fig. 3E**). Furthermore, results showed that *NA* was further downregulated in the combination group (**Fig. 3F**). These trends were consistently observed in FCM results, revealing a substantial increase in GzmB<sup>+</sup> NK cells and GzmB<sup>+</sup> NKT cells within both the EA and combination groups (**Fig. 3G**; Supplementary Fig. S5B). Contrary to the EA and combination groups, the proportion

of GzmB<sup>+</sup>CD8<sup>+</sup> T cells did not increase in the anti-PD-1 group, although the number of CD8<sup>+</sup> T cells was increased (**Fig. 3G**; Supplementary Fig. S5C). These results showed that both EA and combination groups had higher expression of GzmB, indicating stronger cytotoxicity.

Furthermore, our results revealed a notable augmentation in cytotoxic functionality within the combination group compared to EA group, potentially elucidating the enhanced anti-tumor efficacy observed in the EA+aPD1 group. As anticipated, the NK cells in the EA+aPD1 group exhibited elevated expression of *Cd69*, *Prfl*, and *Klrg1*, suggesting enhanced activation and cytotoxic functionality (**Fig. 3H**; Supplementary Fig. S6A). When compared to the EA group, the combination group demonstrated augmented expression of genes associated with CD8 cytotoxic T-cell function (**Fig. 3I**). Additionally, granulocytes in the combination group displayed significantly higher scores in respect to IFN $\alpha$  and IFN $\gamma$  modules, as well as macrophages in respect to pro-inflammatory IFN $\alpha$  and IFN $\beta$  modules (Supplementary Fig. S6B-D). Together, scRNA-seq revealed a markedly augmented anti-tumor immune response in the combination group. Subsequently, we utilized NYG mice to validate the role of the immune system in mediating the anti-tumor effects. NYG immunodeficient mice lack T cells, NK cells, and B cells (Supplementary Fig. S6E-F). Findings indicated that there was no significant difference among the four groups with respect to tumor volume in NYG mice (**Fig. 3J-K**; Supplementary Fig. S6G). In conclusion, our findings demonstrated a noteworthy enhancement in anti-tumor immune responses within the EA and combination groups, with the latter displaying a more robust

cytotoxic function.

### **Electroacupuncture sensitizes tumors to anti-PD-1 and is dependent on STING signaling**

Previous research has suggested that STING signaling pathway can induce the secretion of type I IFN, recruit T cells and NK cells, and sensitize to anti-PD-1 therapy (17). Crucially, we found activation of the STING pathway in the EA group (**Fig. 1K**). Therefore, we further investigated whether the synergy between EA and anti-PD-1 is dependent upon this pathway. As anticipated, both EA and EA+aPD1 treatments activated the STING signaling pathway, as evidenced by substantial increases in pIRF3 and pTBK1 (**Fig. 4A**). Furthermore, IHC analysis revealed a significant increase in IFN $\beta$  secretion within CT26 tumor tissue (**Fig. 4B**). Subsequently, we used STING-deficient mice (*Tmem173<sup>gt</sup>*) to validate the role of STING in this effect, and results indicated that EA failed to enhance the efficacy of anti-PD-1 treatment in MSS CRC (**Fig. 4C-D**; Supplementary Fig. S6H). These findings suggested that EA sensitizes MSS CRC to anti-PD-1 therapy in a STING-dependent manner.

### **Discussion**

ICIs have little clinical efficiency in patients with MSS CRC, and numerous combination strategies aimed to improve responses to anti-PD-1 have unsatisfactory



results. The purpose of this work was to determine whether EA could exert an anti-tumor role and sensitize MSS CRC to anti-PD-1. Here, we first discovered that EA inhibited the growth of MSS tumors in an intensity-specific manner and increased the response to anti-PD-1 by boosting anti-tumor immunity. As shown in previous preclinical studies, EA reduces tumor burden by modulating the neural-endocrine-immune network (11, 13). Our findings indicated that low-frequency EA at ST36 produced a significant anti-tumor effect.

Moreover, results suggested that the decreased expression of NA may mediate the therapeutic effect of EA. NA is known to modulate several important hallmarks of breast cancer, such as immune responses, angiogenesis, and invasion (18). Other acupuncture interventions, such as moxibustion, have also been demonstrated to inhibit tumor growth by regulating adrenergic signaling (14). Interestingly, the intensity of 1.0 mA was more effective than 0.5 or 1.5 mA in MSS CRC mouse models, indicating an optimal intensity for EA-mediated prevention of tumor growth. This may be attributed to the fact that low- and high-intensity EA activate different neural reflexes (9). Previous studies have reported that stimulation of the ST36 using EA at 1.0mA elicits vagus nerve activation, and its activation can significantly enhance anti-tumor immune responses (13). Our research demonstrates for the first time that EA inhibits tumor growth in an intensity-dependent manner. Understanding the precise mechanisms that underlie the efficacy of EA in cancer treatment is imperative for its safe and evidence-based application, due to its growing utilization in clinical practice (7). Our findings are expected to facilitate the effectiveness and

safety of EA treatment for MSS CRC in clinical practice.

The anti-tumor activity of EA was attributed to a potent anti-tumor immune response (11, 13). Our findings revealed that EA substantially increased the proportion of CD8<sup>+</sup> T cells and NK cells, while decreasing the accumulation of MDSCs. Moreover, we first uncovered that EA significantly increased the number of intratumoral GzmB<sup>+</sup> NK cells and GzmB<sup>+</sup> NKT cells. Additionally, we first revealed that EA intervention activated the STING pathway and produced type I IFN, and this associated with recruitment of lymphocytes and contributed to anti-tumor immunity. Mechanistically, this could be explained by the promotion of GzmB-mediated tumor killing, as lytic tumor cells release dsDNA to activate the STING signal pathway (19, 20). Remarkably, research revealed that activation of the STING pathway reprograms the immune TME and sensitizes tumors to anti-PD-1 therapy in malignant melanoma, prostate cancer, and lung cancer (21-23).

Recent research indicates EA might regulate the PD1/PD-L1 pathway (24). Likewise, an increase in PD-L1 expression was observed in our study. This may be caused by the recruitment of CD8<sup>+</sup> T cells and the activation of STING pathway. Importantly, the presence of CD8<sup>+</sup> T cells and PD-L1 is essential for sensitizing to anti-PD-1 therapy (25). In our study, the therapeutic effects of anti-PD-1 were indeed enhanced by EA in both subcutaneous and orthotopic MSS CRC models.

This study is the first to report that EA synergizes with anti-PD-1 immunotherapy in MSS CRC by reshaping TME. Mechanistically, we further revealed that (1) EA

enhanced anti-tumor immune responses by increasing the infiltration of GzmB<sup>+</sup> NK cells, GzmB<sup>+</sup> NKT cells, and CD8<sup>+</sup> T cells, as well as activating the STING pathway; (2) EA induced the expression of PD-L1 as a result of facilitating anti-tumor immunity; (3) EA sensitized tumors to anti-PD-1 therapy through the activation of the STING pathway (**Fig. 4E**). These findings provide the theoretical foundation for a prospective immunotherapy strategy based on anti-PD-1. This innovative combination strategy proves notably beneficial for patients with MSS CRC, which is characterized by limited immunogenicity, especially those without severe impairment of systemic immunity. Our work provides proof-of-concept to establish innovative clinical trials for patients with cold, ICIs non-responsive tumors who are still immunocompetent via the combination of EA with anti-PD-1.

## References

1. Sung H, Ferlay J, Siegel RL, Laversanne M, Soerjomataram I, Jemal A, et al. Global Cancer Statistics 2020: GLOBOCAN Estimates of Incidence and Mortality Worldwide for 36 Cancers in 185 Countries. *CA Cancer J Clin.* 2021;71(3):209-49.
2. Zhou C, Cheng X, Tu S. Current status and future perspective of immune checkpoint inhibitors in colorectal cancer. *Cancer letters.* 2021;521:119-29.
3. Zhao W, Jin L, Chen P, Li D, Gao W, Dong G. Colorectal cancer immunotherapy-Recent progress and future directions. *Cancer letters.* 2022;545:215816.
4. Ma H, Wang H, Sove RJ, Wang J, Giragossian C, Popel AS. Combination therapy with T cell engager and PD-L1 blockade enhances the antitumor potency of T cells as predicted by a QSP model. *Journal for immunotherapy of cancer.* 2020;8(2).
5. Bagchi S, Yuan R, Engleman EG. Immune Checkpoint Inhibitors for the Treatment of Cancer: Clinical Impact and Mechanisms of Response and Resistance. *Annu Rev Pathol.* 2021;16:223-49.
6. Yang SF, Weng MT, Liang JD, Chiou LL, Hsu YC, Lee YT, et al. Neoantigen vaccination augments antitumor effects of anti-PD-1 on mouse hepatocellular carcinoma. *Cancer letters.* 2023;563:216192.
7. Lu L, Zhang Y, Tang X, Ge S, Wen H, Zeng J, et al. Evidence on acupuncture therapies is underused in clinical practice and health policy. *BMJ (Clinical research ed).* 2022;376:e067475.
8. Torres-Rosas R, Yehia G, Peña G, Mishra P, del Rocio Thompson-Bonilla M,

Moreno-Eutimio MA, et al. Dopamine mediates vagal modulation of the immune system by electroacupuncture. *Nature medicine*. 2014;20(3):291-5.

9. Liu S, Wang ZF, Su YS, Ray RS, Jing XH, Wang YQ, et al. Somatotopic Organization and Intensity Dependence in Driving Distinct NPY-Expressing Sympathetic Pathways by Electroacupuncture. *Neuron*. 2020;108(3):436-50 e7.

10. Xu X, Feng X, He M, Zhang Z, Wang J, Zhu H, et al. The effect of acupuncture on tumor growth and gut microbiota in mice inoculated with osteosarcoma cells. *Chinese medicine*. 2020;15:33.

11. Li S, Zhao S, Guo Y, Yang Y, Huang J, Wang J, et al. Clinical Efficacy and Potential Mechanisms of Acupoint Stimulation Combined With Chemotherapy in Combating Cancer: A Review and Prospects. *Front Oncol*. 2022;12:864046.

12. Mao JJ, Liou KT, Baser RE, Bao T, Panageas KS, Romero SAD, et al. Effectiveness of Electroacupuncture or Auricular Acupuncture vs Usual Care for Chronic Musculoskeletal Pain Among Cancer Survivors: The PEACE Randomized Clinical Trial. *JAMA oncology*. 2021;7(5):720-7.

13. Zhang Z, Yu Q, Zhang X, Wang X, Su Y, He W, et al. Electroacupuncture regulates inflammatory cytokines by activating the vagus nerve to enhance antitumor immunity in mice with breast tumors. *Life Sci*. 2021;272:119259.

14. Hu D, Shen W, Gong C, Fang C, Yao C, Zhu X, et al. Grain-sized moxibustion promotes NK cell antitumour immunity by inhibiting adrenergic signalling in non-small cell lung cancer. *Journal of cellular and molecular medicine*. 2021;25(6):2900-8.

15. Stone JA, Johnstone PA. Mechanisms of action for acupuncture in the oncology setting. *Current treatment options in oncology*. 2010;11(3-4):118-27.
16. Song W, Shen L, Wang Y, Liu Q, Goodwin TJ, Li J, et al. Synergistic and low adverse effect cancer immunotherapy by immunogenic chemotherapy and locally expressed PD-L1 trap. *Nat Commun*. 2018;9(1):2237.
17. Mondal I, Das O, Sun R, Gao J, Yu B, Diaz A, et al. PP2Ac Deficiency Enhances Tumor Immunogenicity by Activating STING-Type I Interferon Signaling in Glioblastoma. *Cancer Res*. 2023;83(15):2527-42.
18. Yu S, Li W, Tang L, Fan X, Yao S, Zhang X, et al. Depression in breast cancer patients: Immunopathogenesis and immunotherapy. *Cancer letters*. 2022;536:215648.
19. Morel KL, Sheahan AV, Burkhart DL, Baca SC, Boufaied N, Liu Y, et al. EZH2 inhibition activates a dsRNA-STING-interferon stress axis that potentiates response to PD-1 checkpoint blockade in prostate cancer. *Nat Cancer*. 2021;2(4):444-56.
20. Marcus A, Mao AJ, Lensink-Vasan M, Wang L, Vance RE, Raulet DH. Tumor-Derived cGAMP Triggers a STING-Mediated Interferon Response in Non-tumor Cells to Activate the NK Cell Response. *Immunity*. 2018;49(4):754-63.e4.
21. Zhou L, Xu Q, Huang L, Jin J, Zuo X, Zhang Q, et al. Low-dose carboplatin reprograms tumor immune microenvironment through STING signaling pathway and synergizes with PD-1 inhibitors in lung cancer. *Cancer letters*. 2021;500:163-71.
22. He L, Xiao X, Yang X, Zhang Z, Wu L, Liu Z. STING signaling in tumorigenesis and cancer therapy: A friend or foe? *Cancer letters*. 2017;402:203-12.
23. Ma S, Caligiuri MA, Yu J. Harnessing Natural Killer Cells for Lung Cancer

Therapy. *Cancer Res.* 2023.

24. Wu Q, Zheng Y, Yu J, Ying X, Gu X, Tan Q, et al. Electroacupuncture alleviates neuropathic pain caused by SNL by promoting M2 microglia polarization through PD-L1. *Int Immunopharmacol.* 2023;123:110764.

25. Sanmamed MF, Chen L. A Paradigm Shift in Cancer Immunotherapy: From Enhancement to Normalization. *Cell.* 2018;175(2):313-26.

## **Figure Legends**

### **Figure 1**

**EA exhibits its anti-tumor efficacy in a manner that is specific to its intensity and significantly increases immune response.** **A**, Schematic diagram of the EA treatment. 10 days post CT26 tumor cell injection (i.p.), BALB/c mice were randomized into five groups: (1) Control; (2) Sham EA; (3) 0.5 mA EA; (4) 1.0 mA EA; (5) 1.5 mA EA. EA was used to stimulate the bilateral Zusanli acupoint (ST36) once a day for 14 days. **B**, Representative image of CT26 tumors in BALB/c mice after 14 days of treatment (n=8). **C**, Tumor growth curves with mean tumor volumes  $\pm$  SEM (n=8). A two-way ANOVA with Dunnett's multiple comparisons test was used. **D** and **E**, Tumor tissues from CT26 tumor-bearing mice treated with control or 1.0 mA EA were analyzed for immune cell infiltration after 14 days of treatment. Representative flow cytometry plots of intratumoral frequencies of CD8<sup>+</sup>T (**D**) and NK cells (**E**) (n = 4). **F**, Serum levels of noradrenaline, adrenaline and dopamine were analyzed by ELISA (n=3). **G**, The bubble diagram of GO enrichment analysis displays the top 30 terms that enriched in 1.0 mA EA group. **H**, Representative immunostaining images of tumor sections from CT26 tumor-bearing mice stained for GzmB, IFN- $\beta$ , and PD-L1 (up). Quantitative analysis of GzmB, PD-L1, and IFN- $\beta$  IHC staining intensity (down) (n=3). **I**, The mRNA levels of GzmB and PD-L1 were measured by qRT-PCR. Data are normalized to  $\beta$ -actin expression levels. Total RNA was extracted from CT26 tumor tissues (n=3). **J**, The serum level of IFN- $\beta$  was detected by ELISA (n=6). **K**, WB showed the expression of pIRF3 and pTBK1 which are involved in the STING



pathway (n=3). Representative data from two experiments with at least six mice are shown (**B** and **C**). Data are expressed as the mean  $\pm$  SEM. The indicated sample size (n) represents biological replicates. \* P<0.05, \*\* P<0.01, \*\*\* P<0.001, \*\*\*\* P<0.0001. Abbreviations: EA, electroacupuncture; SEM, standard error of mean; NK, natural killer; ELISA, enzyme-linked immunosorbent assay; GO, gene ontology; BP, biological process; CC: cellular component; MF: molecular function; ANOVA, one-way analysis of variance; GzmB, granzyme B; IFN $\beta$ , interferon-beta; IHC, immunohistochemistry; qRT-PCR, quantitative real-time PCR; WB, western blotting; STING, stimulator of interferon genes.

## Figure 2

**EA sensitized anti-PD-1 in multiple mouse models of MSS CRC.** **A**, Summary of experimental design to study the therapeutic effect of combination treatment in CT26 tumor-bearing mouse. Once tumors reached an average volume of  $\sim 100\text{--}200\text{mm}^3$  on day 10, BALB/c mice were randomized into four groups: (1) Control; (2) EA stimulation; (3) aPD1; (4) EA+aPD1. aPD1 was administered via the i.p. route. **B**, Representative image of CT26 tumors in BALB/c mice after 14 days of treatment (n=6). **C**, Tumor growth curves with mean tumor volumes  $\pm$  SEM (n=6). A two-way ANOVA with Dunnett's multiple comparisons test was used. **D**, Bar graphs showed the individual changes in tumor growth relative to after and before treatment. **E**, Kaplan-Meier survival curves were shown (n=6). **F**, Bioluminescent imaging for CT26-luc orthotopic colon tumors at different time points. **G**, Tumor growth was

monitored by luminescence and plotted as the average radiance (n=3). Data are representative of at least two independent experiments and expressed as the mean  $\pm$  SEM. The indicated sample size (n) represents biological replicates. \* P<0.05, \*\* P<0.01, \*\*\* P<0.001, \*\*\*\* P<0.0001. Abbreviations: EA, electroacupuncture; MSS CRC, microsatellite-stable colorectal cancer; i.p. intraperitoneal; SEM, standard error of mean; ANOVA, one-way analysis of variance.

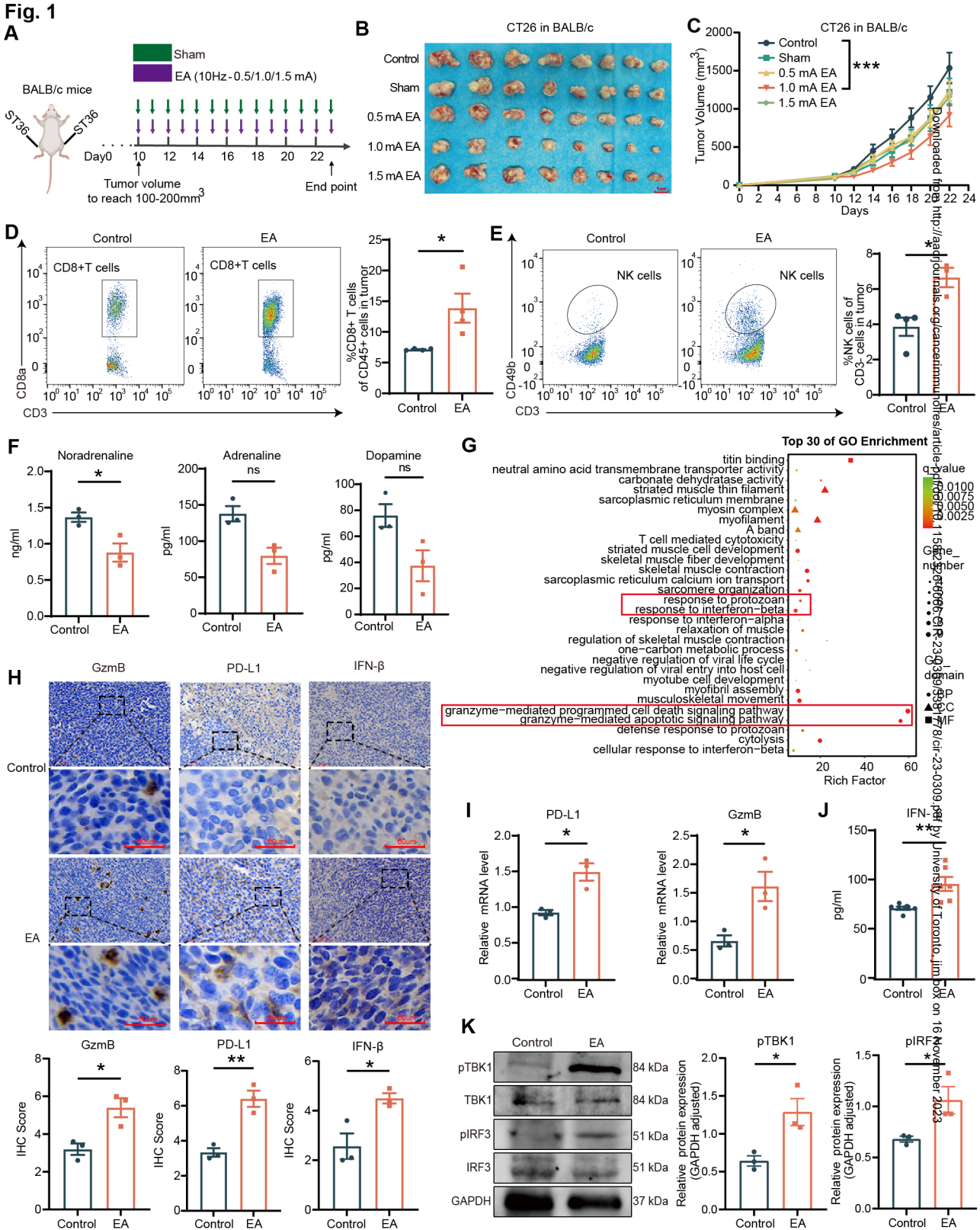
### Figure 3

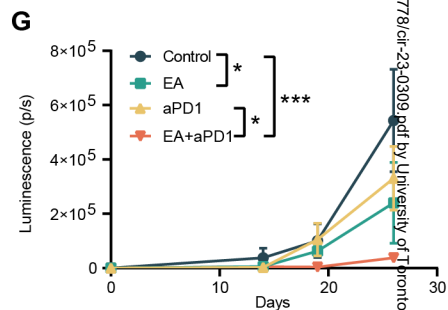
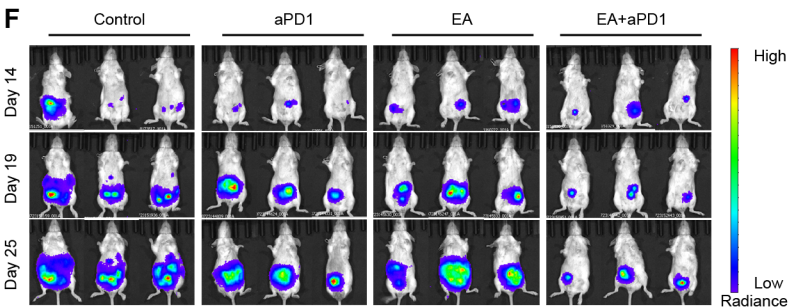
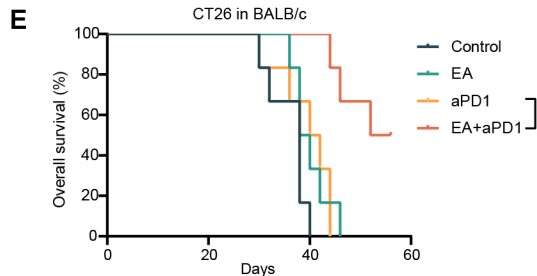
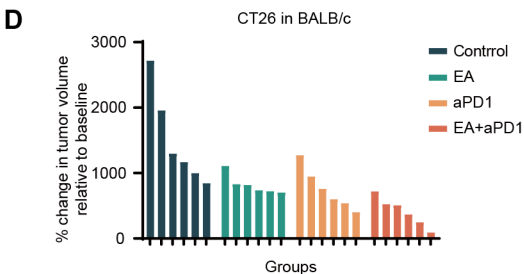
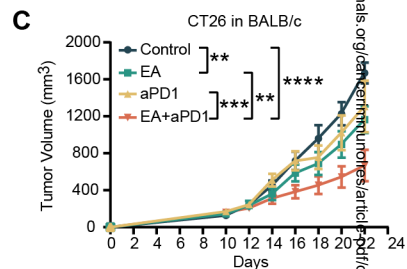
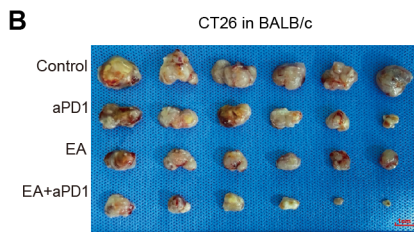
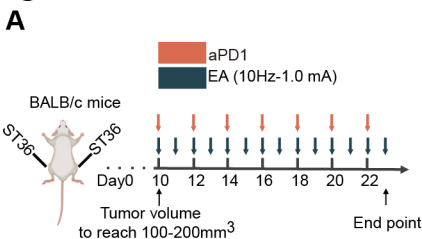
**Single-cell RNA sequencing illustrated the strengthened anti-tumor immunity observed in the combination group.** **A**, t-SNE projection of cell clusters in CT26 tumor-bearing mice. **B**, Graph showed the relative proportion of each immune cell subpopulation. **C**, Percentages of NK, NKT and CD8<sup>+</sup> T cells in tumor tissues determined by FCM after 14 days of treatment (n=4). **D**, GzmB expression in each lymphocyte subset. **E**, Adrb1 and Adrb2 expressions in each lymphocyte subset. **F**, The serum level of NA in blood (n=3). **G**, CT26 tumor tissues were analyzed for immune cell infiltration after 14 days of treatment. The proportions of GzmB<sup>+</sup> NK, GzmB<sup>+</sup> NKT, and GzmB<sup>+</sup>CD8<sup>+</sup> T cells in CT26 tumors (n=4). **H**, Normalized expressions of Cd69 and Prf1 on NK cells were shown. **I**, The module score of CD8<sup>+</sup> cytotoxic T lymphocyte function. **J**, Tumor growth curves of CT26 tumors in NYG mice were shown (n=6). A two-way ANOVA with Dunnett's multiple comparisons test was used. **K**, Fold tumor volume change compared to initial tumor volume. Representative data from two experiments with at least six mice were shown (**J** and

**K**). Data are expressed as the mean  $\pm$  SEM. The indicated sample size (n) represents biological replicates. \*  $P < 0.05$ , \*\*  $P < 0.01$ , \*\*\*  $P < 0.001$ , \*\*\*\*  $P < 0.0001$ . Abbreviations: NK, natural killer; NKT, natural killer T; ANOVA, one-way analysis of variance; SEM, standard error of mean.

#### **Figure 4**

**EA enhanced the efficacy of anti-PD-1 in a STING-dependent manner. A**, WB analysis of pTBK1 and pIRF3 expression in tumor tissues (n=3). **B**, Representative IHC images of IFN- $\beta$  and quantitative analysis of the intensity of IFN- $\beta$  staining in the IHC images (n=3). Scale bar, 60  $\mu$ m. **C**, Fold tumor volume change compared to initial tumor volume (n=5). **D**, Tumor growth curves of CMT93 tumor in *Tmem173<sup>gt</sup>* mice (n=5). A two-way ANOVA with Dunnett's multiple comparisons test was used. **E**, Schema of the major results and interpretation of this study. Representative data from two experiments with at least five mice are shown (**D**). Data are expressed as the mean  $\pm$  SEM. The indicated sample size (n) represents biological replicates. \*  $P < 0.05$ , \*\*  $P < 0.01$ , \*\*\*  $P < 0.001$ , \*\*\*\*  $P < 0.0001$ . Abbreviations: EA, electroacupuncture; STING, stimulator of interferon genes; WB, western blotting; IHC, immunohistochemistry; IFN- $\beta$ , interferon-beta; ANOVA, one-way analysis of variance; SEM, standard error of mean.



**Fig. 2**

**Fig. 3**

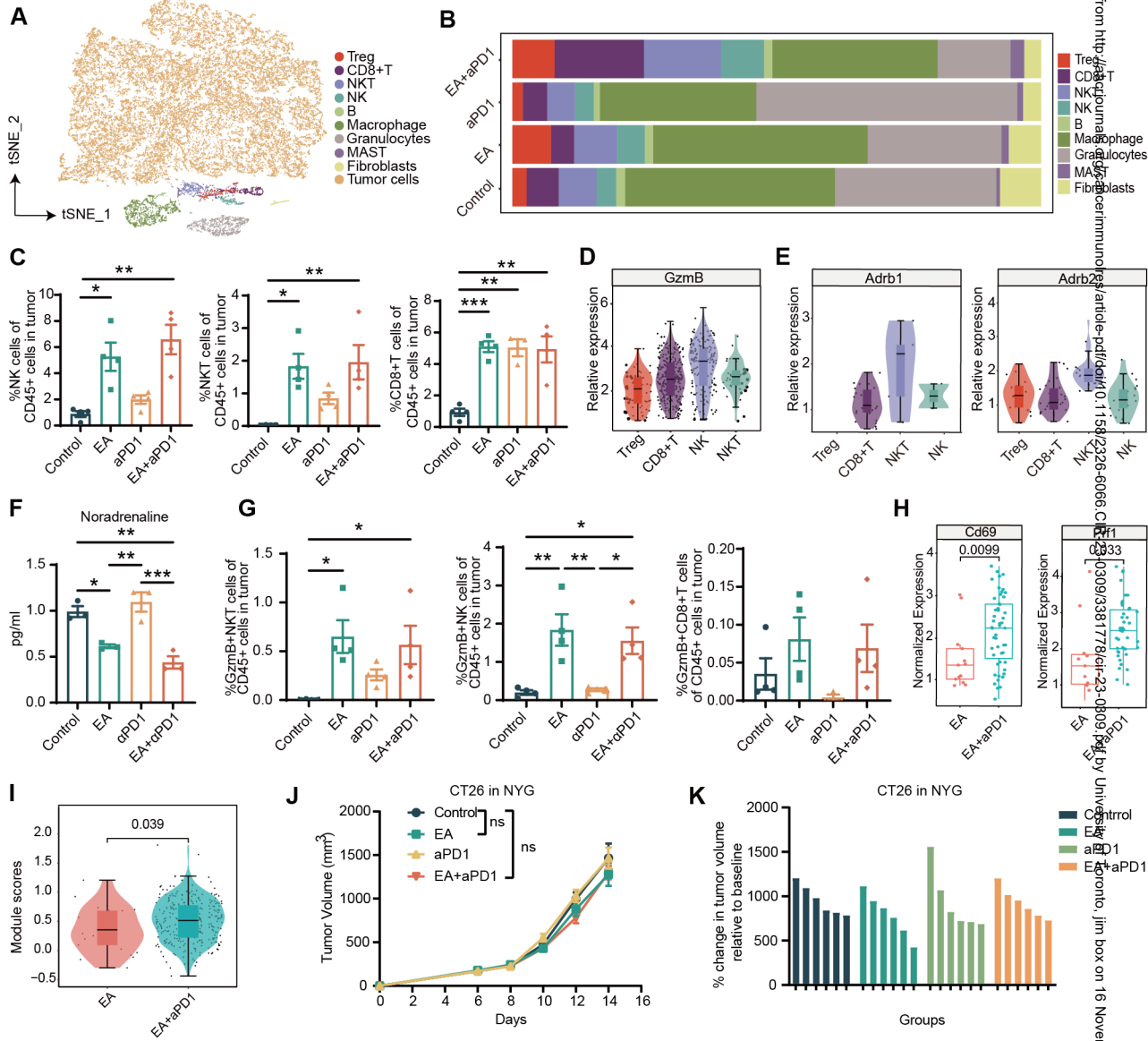


**Fig. 4**

